Chapter 6
Manifestations of Hydrogen Embrittlement

Internal cracking such as blistering is, historically and still in the present, a typical hydrogen problem for structural steel components. Blistering is induced under high hydrogen fugacity even without external stress, but degradation or eventually failure of structural steel components emerges in use under mild atmospheric environments. It is to be noticed that the function of hydrogen in the degradation is coupled with applied stress and plastic strain. In this section, mostly phenomenological manifestations of hydrogen effects in various mechanical testing of steels are presented.

6.1 Tensile Tests

(a) Phenomenological features

At tensile tests using bulky specimens, hydrogen degradation appears as premature fracture after or eventually before necking in the apparently elastic region close to the yield stress according to materials, hydrogen concentrations and testing conditions. The degradation is expressed in terms of the fracture stress, the elongation to fracture and the reduction in area. Figure 6.1 [1] shows stress–strain curves of high strength steel bar specimens of 3 mm in diameter with and without hydrogen precharging. The microstructure of the steel (0.84C-0.19Si-0.76Mn in %) was lower bainite of 1517 MPa in tensile strength and was hydrogen precharged by immersing specimens in a 20 % aqueous solution of NH_4SCN at 50 °C for various periods to control hydrogen concentrations. The tensile tests were conducted at room temperature with the strain rate of 5×10^{-7}/s.

The hydrogen concentration increased with the immersion time and tended to saturate at about 3 mass ppm after 10 h. Thermal desorption analysis (TDA) profiles of hydrogen exhibited a single desorption-rate peak at around 120 °C, suggesting that hydrogen is weakly trapped in lattice defects as described in Sect. 2.1.2.

M. Nagumo, *Fundamentals of Hydrogen Embrittlement*,
DOI 10.1007/978-981-10-0161-1_6

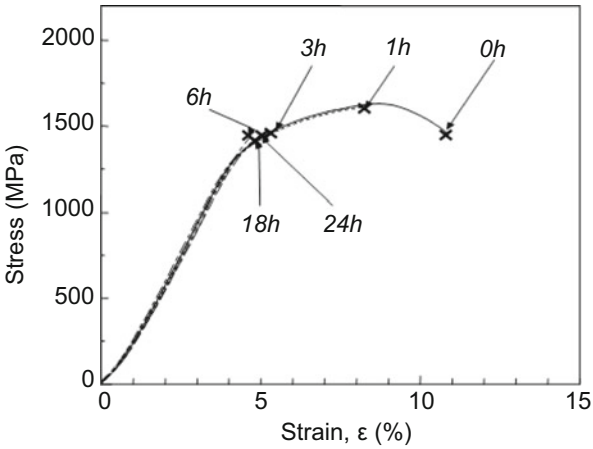

Fig. 6.1 Tensile stress–strain curve of a high-strength lower-bainitic steel with/without hydrogen precharging by immersion in 20 % NH_4SCN solution at 50 °C for various periods. Test at room temperature at a strain rate of 5×10^{-7}/s (Takai et al. [1]. Reprinted with permission from The Iron & Steel Inst. Japan)

Actually hydrogen almost totally diffused out at room temperature in 800 h. A good correlation was revealed between the increase in hydrogen concentrations and the degradation in tensile properties shown in Fig. 6.1.

Alternatively, the steel of the same compositions was isothermally transformed at 550 °C to eutectoid structure and was given cold-drawing to 85 % reduction in area [1]. Hydrogen precharging was conducted in the same way as for the lower bainite steel in Fig. 6.1. TDA profiles of hydrogen exhibited two peaks at around 120 °C (Peak$^{\#1}$) and 350 °C (Peak$^{\#2}$) similarly to Fig. 2.4, and each peak increased with the immersion time. Specimens containing only Peak$^{\#2}$ hydrogen were prepared by annealing cold-drawn and hydrogen-charged specimens at 200 °C. It indicates that hydrogen composing Peak$^{\#2}$ is strongly trapped and non-diffusive even at 200 °C. As shown shortly in Fig. 6.4, tensile tests of thus annealed specimens revealed that hydrogen composing Peak$^{\#2}$ is immune to degradations. It implies that the total hydrogen content does not serve as a parameter for the degradation of tensile properties.

For hydrogen embrittlement of steels, the stage in which the onset of fracture takes place is important for considering the function of hydrogen. Figure 6.2(a) [2] is an example of tensile stress–strain curves of Type 304 and Type 316 L austenitic stainless steels at room temperature with and without hydrogen precharging. Hydrogen was uniformly precharged in 10 MPa hydrogen gas at 400 °C to about 35 mass ppm. Hydrogen degradation appeared for Type 304 steel and fracture took place apparently discontinuous in the uniform elongation stage. However, careful examination revealed that the load drop was rather continuous as shown in Fig. 6.2(b). Since the strain rate was 8.3×10^{-4}/s, elongation of 0.5 % spent about 1 min. The finding suggests that hydrogen promotes the onset of plastic instability, but the diffusion of hydrogen is not likely to cause the instability since diffusion of hydrogen in austenitic stainless steels is almost negligible during the test at room temperature. Related descriptions on the event are made in Sects. 7.2.1(b) and 8.4.4 about strain localization and in Sect. 10.5 about its role in the mechanism of hydrogen embrittlement.

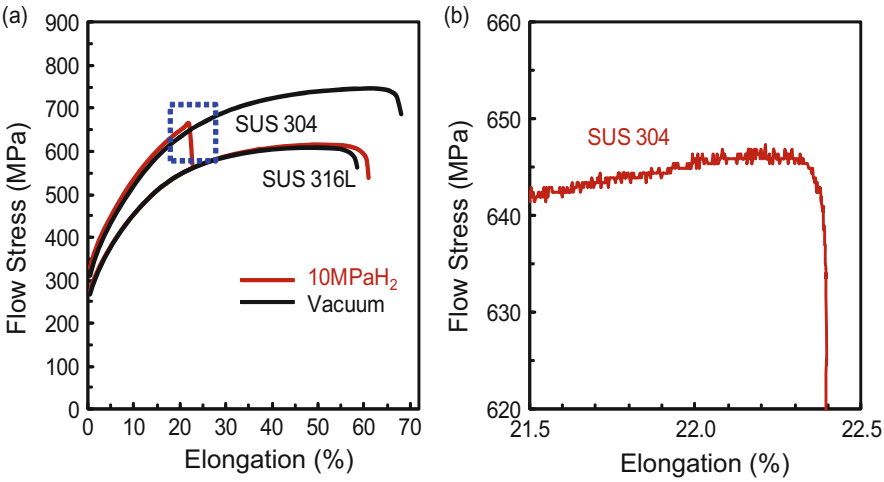

Fig. 6.2 (**a**) Stress–strain curves of Type 304 and Type 316 L stainless steels with/without hydrogen pre-charging. (**b**) A magnified view of the curve near the load-drop of hydrogen-charged Type 304 (Hatano et al. [2])

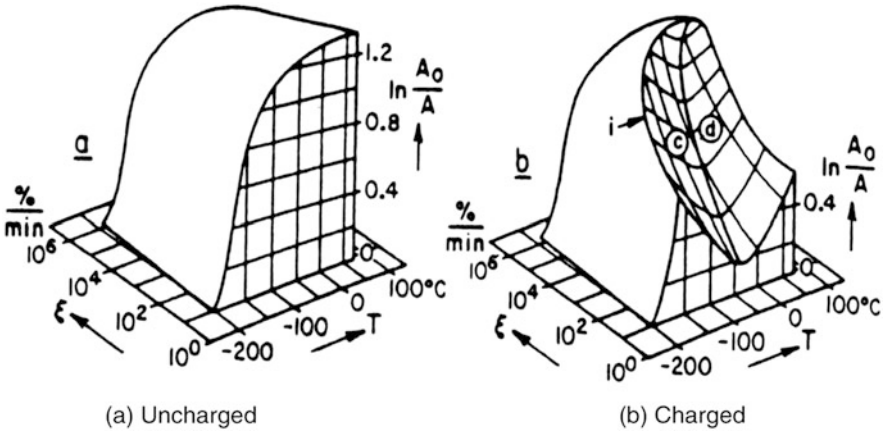

Fig. 6.3 Schematic diagram for the effects of strain rate and temperature on tensile properties of mild steel with and without hydrogen (Bernstein [3]. Reprinted with permission from TMS)

(b) Involvement of strain-induced vacancies in degradation

Strain rate and testing temperature dependencies characterize the susceptibility to hydrogen embrittlement of steels in tensile tests. Figure 6.3 [3] schematically illustrates the dependencies of fracture strain in terms of the reduction in area at fracture for mild steel. The degradation is the most prominent at around room temperature and with decreasing strain rates. A common understanding so far on the origin is the rate of buildup of local hydrogen concentration through diffusion.

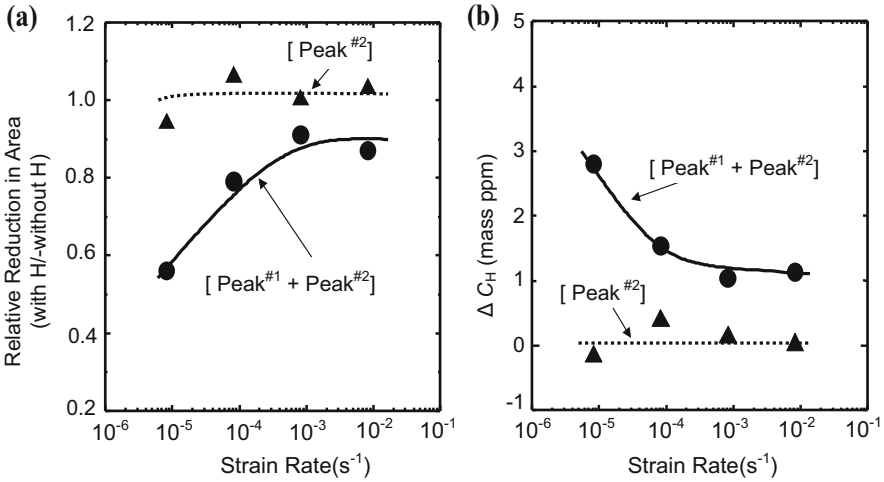

Fig. 6.4 Strain rate dependencies of (**a**) relative reduction in area at tensile tests for specimens containing [Peak$^{\#1}$ + Peak$^{\#2}$] hydrogen and only [Peak$^{\#2}$] hydrogen, (**b**) difference of Peak$^{\#1}$ hydrogen, ΔC_H, between specimens strained to 0.08 with and without hydrogen for [Peak$^{\#1}$ + Peak$^{\#2}$] and [Peak$^{\#2}$] series (Doshida et al. [4])

On the other hand, the origin of the dependencies was studied by means of TDA that gave information on the states of hydrogen in materials [4].

As described in the preceding Sect. 6.1(a), hydrogen introduced into cold-drawn eutectoid steel bars exhibit two thermal desorption-rate peaks, Peak$^{\#1}$ and Peak$^{\#2}$. Tensile test results for the two series of specimens, one containing both Peak$^{\#1}$ and Peak$^{\#2}$ and the other containing only Peak$^{\#2}$, are shown in Fig. 6.4(a) [4] at various strain rates. The ordinate denotes the ratio of reduction in area at tensile tests of steels with and without hydrogen precharging. Hydrogen degradation and a strong strain rate dependence of tensile ductility appeared for specimens containing Peak$^{\#1}$ hydrogen while specimens containing only Peak$^{\#2}$ were almost immune.

The amounts of lattice defects newly created during tensile straining were evaluated in terms of the amount of tracer-hydrogen introduced to saturation into specimens after tensile straining. Since Peak$^{\#1}$ hydrogen was crucial to embrittlement, the amounts of tracer-hydrogen in strained specimens initially containing [Peak$^{\#1}$ + Peak$^{\#2}$] or only [Peak$^{\#2}$] were measured by TDA. The enhancement by hydrogen of strain-induced creation of defects was expressed in terms of ΔC_H defined as the difference in Peak$^{\#1}$ tracer-hydrogen between specimens strained to 0.08 with and without hydrogen. Figure 6.4(b) [4] shows ΔC_H for [Peak$^{\#1}$ + Peak$^{\#2}$] and only [Peak$^{\#2}$] series at different strain rates. The ΔC_H for [Peak$^{\#1}$ + Peak$^{\#2}$] series increased at lower strain rates, but it was independent of strain rates for [Peak$^{\#2}$] series. The results correspond well to the degradation of tensile ductility shown in Fig. 6.4(a). Hydrogen effects are relevant to the enhanced creation of strain-induced defects composing Peak$^{\#1}$, and the strain rate dependence of degradation is associated with the amount of strain-induced defects. The strain rate

dependence is also shown in Figs. 7.18 and 7.19 in Sect. 7.3.2 for effects of cyclic prestressing. The vacancy-type entity of lattice defects relevant to the strain-induced increase in Peak$^{\#1}$ hydrogen is described for Fig. 3.10 in Sec. 3.2.3(b) about low temperature thermal desorption spectroscopy.

Similar experiments were conducted for the temperature dependence of tensile ductility [4]. The hydrogen-enhanced loss of ductility appeared significantly with increasing test temperatures from −50 °C to 75 °C for specimens containing Peak$^{\#1}$ hydrogen, while the ductility of specimens containing only Peak$^{\#2}$ were almost immune to hydrogen. The temperature range in which the increase in ΔC_H appeared for [Peak$^{\#1}$ + Peak$^{\#2}$] series was coincident with that for the loss of ductility.

Positron annihilation spectroscopy was further successfully applied to discriminate lattice defects involved in the strain rate effect [5, 6]. Positron lifetime in strained pure iron exhibited a long lifetime component exceeding 250 ps when hydrogen was precharged. The component corresponded to vacancy clusters and its relative intensity increased with decreasing strain rates in accord with the behavior of ΔC_H. It is a complementary and more direct support for the notion that the strain rate dependence of the susceptibility to hydrogen embrittlement is closely related to the strain-induced creation of vacancies and their clusters.

Discussion on the function of hydrogen in embrittlement has addressed mostly the initiation and growth of cracks in late stages of deformation. However, it was demonstrated for iron and Inconel 625 that hydrogen is not necessarily requisite for embrittlement in the late stage of deformation [7]. The experiments were to interpose unloading and reloading during tensile tests of hydrogen-precharged specimens as schematically shown in Fig. 6.5 [7]. Unloading was applied at

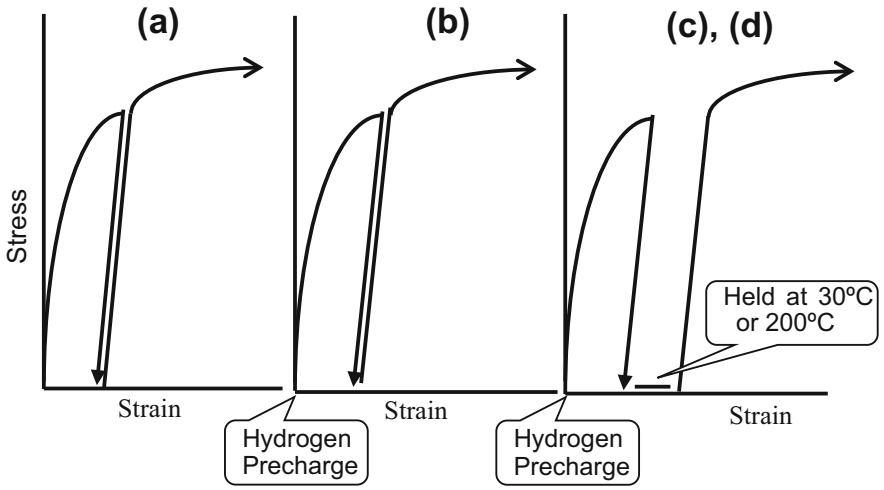

Fig. 6.5 Procedures of interposed unloading and reloading during tensile test. (**a**) Immediate reloading after unloading without hydrogen precharging. (**b**) Hydrogen precharged and immediate reloading after unloading. (**c**) Hydrogen precharged and aged at 30 °C or (**d**) at 200 °C after unloading (Takai et al. [7])

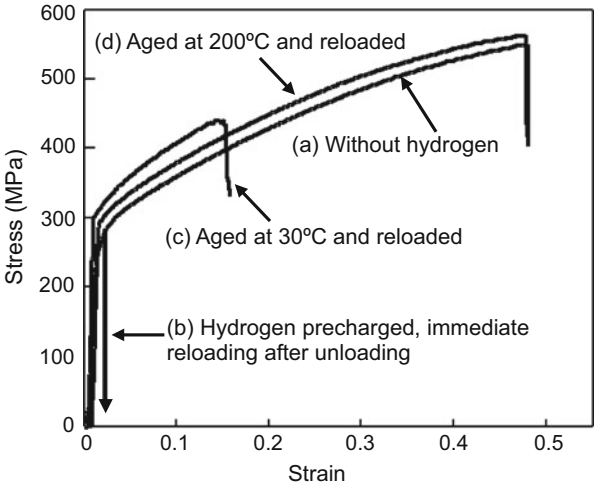

Fig. 6.6 Stress–strain curves of Inconel 625 at tensile tests with interposed unloading shown in Fig. 6.5 (Takai et al. [7])

about a half of or close to the fracture strain for iron or Inconel 625, respectively, and degassing at 30 °C or annealing at 200 °C was conducted at the unloaded stage.

Figure 6.6 [7] shows tensile curves of Inconel 625 after reloading. Hydrogen precharging degraded substantially tensile properties and the interposed unloading did not affect the degradation in the hydrogen-charged specimen when reloaded immediately. On the other hand, a substantial degradation remained while hydrogen was removed at the unloaded stage and complete recovery of the degradation appeared by annealing at 200 °C at the unloaded stage. The result demonstrates that the hydrogen-enhanced creation of strain-induced vacancies (HESIV), rather than hydrogen itself, plays the essential role in the degradation.

6.2 Fracture Mechanics Tests

Fracture toughness of materials is evaluated by means of various fracture mechanics test methods using notched or precracked specimens. Charpy impact tests are not appropriate for evaluating hydrogen embrittlement because of involved high strain rate. Fracture toughness is expressed in terms of various quantities such as stress intensity factor (K), crack-opening displacement (COD), and J-integral [8, 9]. In hydrogen or hydrogen-producing environments, the macroscopic crack initiates at the notch-root or the tip of the precrack. The initiation and slow growth rates of cracks are schematically shown in Fig. 6.7 as a function of applied K. Below a threshold stress intensity K_{TH}, crack growth is negligible and K_{TH} is usually denoted as K_{ISCC} for stress corrosion cracking under plane strain condition. Crack growth rates generally exhibit three stages. The growth rate in Stage II is much lower than in Stage I or insensitive to K. Stage III corresponds to final fracture when K reaches the fracture toughness K_c of the material. In sustained-load testing at a

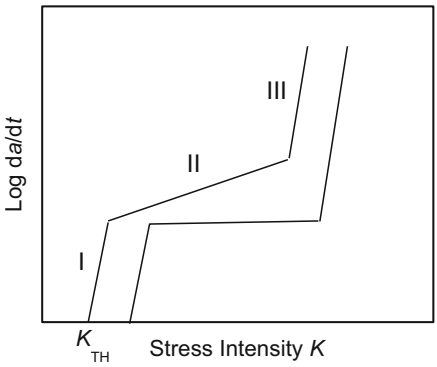

Fig. 6.7 Schematic diagram of three stages of slow crack growth rates with increasing stress intensity

constant applied stress, K increases with the crack growth. On the other hand, K decreases with the crack growth in constant displacement loading. Another threshold stress intensity for crack arrest K_{th} is the value at which the crack growth ceases. Fracture mechanics tests normally need bulky specimens, and inhomogeneous distribution of hydrogen makes the exact estimation of the hydrogen concentration difficult at active sites in the specimen for fracture.

6.2.1 Crack Initiation

The initiation and growth of a crack are detected for fatigue-precracked wedge-opening-load (WOL), compact tension (CT) and double cantilever beam (DCB) specimens under controlled environments [10–14]. The crack growth rate is measured directly [12, 13] or is calculated from the time record of compliance of the specimen [10–14]. Crack growth kinetics varies with the strength level, hydrogen concentration and temperature. Data of threshold stress intensities for the crack initiation in hydrogen gas were compiled by Moody and Robinson as shown in Fig. 6.8 [15] for AISI steels of different yield strengths. The K_{TH} values are strongly dependent on the yield strength and decrease to some limiting values with elevated hydrogen gas pressure. An observed relationship between K_{TH} and P_{H2} at room temperature for an AISI 4340 steel of 1240 MPa in yield strength was [10]

$$K_{TH} = 151 - 60 \log P_{H_2} \quad (15 < P_{H_2} < 115), \tag{6.1}$$

where P_{H2} was in unit of 6.89 kPa and K_{TH} was in unit of 1.1 MPa·m$^{1/2}$. However, a lower limit existed for K_{TH} at high hydrogen gas pressures above about 690 kPa. The pressure dependence of K_{TH} is strongly dependent on the yield stress of steels, and the dependence is also sensitive to the magnitude of K_{TH} as shown in Fig. 6.8.

The value of K_{TH} increases with the rise of temperature [10, 15]. Low K_{TH} values at room temperature correspond to Fig. 6.3 for tensile ductility. The

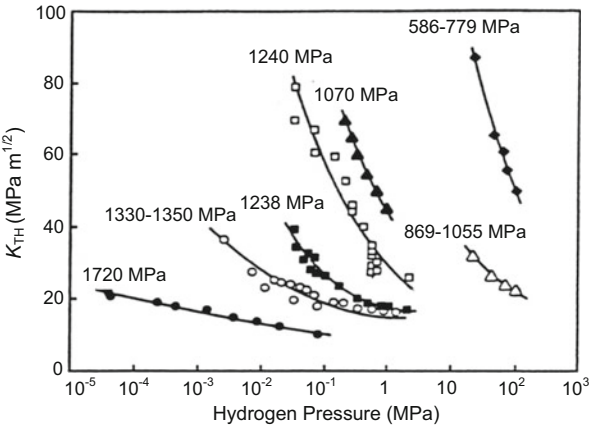

Fig. 6.8 Effects of hydrogen pressure on the threshold stress intensity K_{TH} for crack initiation for AISI 4340 steel (yield strength in MPa) (Moody et al. [15])

dependence differs by steels and magnitudes of K_{TH}. An Arrhenius relationship that indicates a thermally activated process for the same steel as used for Eq. (6.1) in 551 kPa hydrogen was [10],

$$K_{TH} = 3631\exp\left(-1471/T\right) \quad (298 < T(K) < 480)\,, \tag{6.2}$$

where K_{TH} was in unit of 1.1 MPa·m$^{1/2}$.

The K_{TH} values are lower for higher strength steels at a given hydrogen gas pressure. The yield strengths of the steels shown in Fig. 6.8 were controlled through microstructural alterations by tempering temperatures. Micro-plasticity at the crack front should play the role in the degradation, but the intrinsic factor or microscopic process that controls such dependencies is not simple.

The values of K_{TH} were determined by modified WOL tests from the stationary value of the load reached after decreasing with time from the load at which a load drop took place on step loading [16]. Takeda and McMahon noticed with measurements for a 5 % Ni HY 130 steel in hydrogen gas that a subtle crack initiation actually took place along the periphery of plastic hinge or slip lines well below the detectable K_{TH} on loading [16]. Related descriptions concerning impurity effects are in Sect. 8.2(a).

Stress and strain fields in front of the crack tip are expressed in terms of the stress intensity, but the method has limitations when crack-tip plasticity extends. The quantities COD and J-integral are then employed to properly evaluate fracture toughness for medium strength steels. The J-integral is a path-independent integral along an arbitrary counterclockwise path Γ around the tip of crack and is defined as

$$J = \int_{\Gamma} \left(w dy - T_i \frac{\partial u_i}{\partial x} ds \right), \tag{6.3}$$

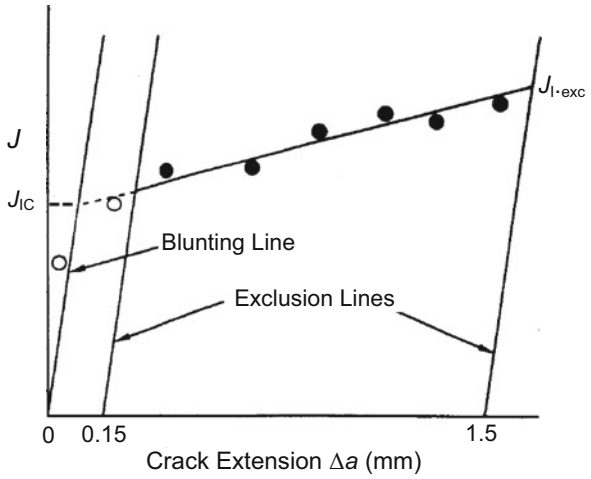

Fig. 6.9 A typical Mode I *J*-resistant curve for a pure mode I test (Gordon et al. [17])

where w is the strain energy density, T_i is the i-th component of the traction vector, u_i is the i-th component of displacement vector and ds is the length increment along the contour Γ. The J-integral is a measure of the energy dissipated per unit length of crack tip per unit distance of crack advance and is experimentally obtained from the specimen geometries and the area of the load *vs.* load-point displacement curve.

The J-integral value at the onset of a stable crack growth, J_{TC}, is determined as the intersection of the crack blunting line with the J *vs.* Δa curve. For pure mode I loading, J_{TC} is denoted as J_{IC} as shown in Fig. 6.9 [17]. In many practical situations, multiple loading modes superpose, and mode III loading causes localized shear ahead of the crack tip, and an empirical correlation which relates the mixed-mode fracture toughness to the process zone size was proposed [18]. Hydrogen effects on mixed mode I/III fracture toughness were examined for a high purity Ni-Cr-Mo-V steel of tempered lower bainitic structure and 855 MPa in tensile strength [17]. Hydrogen was precharged in 13.8 MPa hydrogen gas at 100 °C to a hydrogen concentration of 2 at. ppm equivalent to a hydrogen fugacity of 1.26 GPa at room temperature. In order to adjust the shear stress component, CT specimens with a slant notch of varied angle Φ were used. Figure 6.10 [17] shows that the increasing mode III component decreases J_{TC} in both hydrogen-charged and uncharged conditions and that hydrogen enhances the degradation additionally by about 30 %. The fracture surface exhibited smaller and more uniform dimples with the increase in the mode III loading component. The findings imply that plasticity plays a role in the crack initiation and that hydrogen is incorporated in the degradation through plasticity. The mechanistic explanation of the finding is described in Sect. 10.4.

Experimental determination of the crack initiation from the precrack is often not precise for medium strength steels. A method for detecting the onset of a stable crack growth from the precrack tip was devised [19] by recording the progress of crack-tip opening displacement δ according to the theory by Needleman and

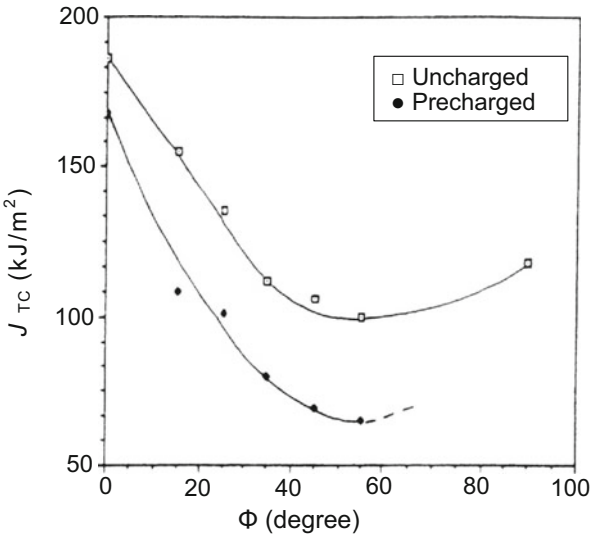

Fig. 6.10 A plot of J_{TC}*vs.* tilting angle Φ showing J_{TC} decreasing with increasing mode III loading (Gordon et al. [17])

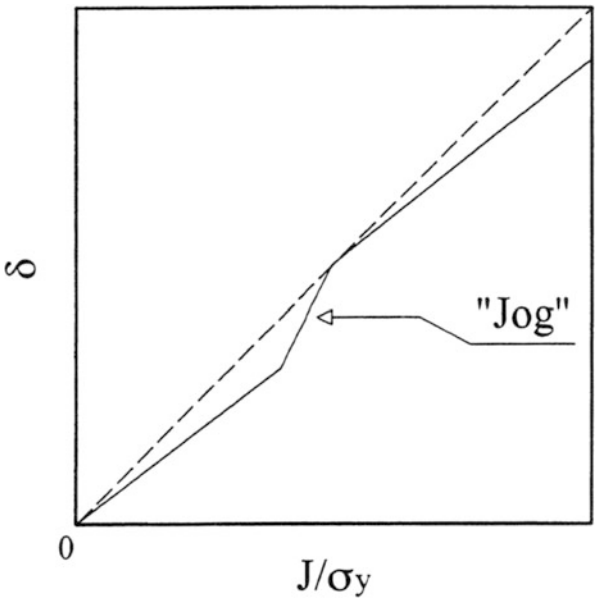

Fig. 6.11 Schematic illustration of the appearance of a "jog" on crack opening displacement δ *vs.* J-integral normalized by yield stress

Tvergaard [20] described in Sect. 10.1.3. The onset of the stable crack growth expects a discontinuous increase in δ accompanying a jog to appear on the δ vs J-integral curve. However, the jog will be too small to be detected directly. Alternatively, the gradient of the curve is more sensitive to the appearance of a jog as schematically shown in Fig. 6.11. The method was applied to a three-point bending test of notched specimens of a low carbon steel of 450 MPa in tensile strength. The

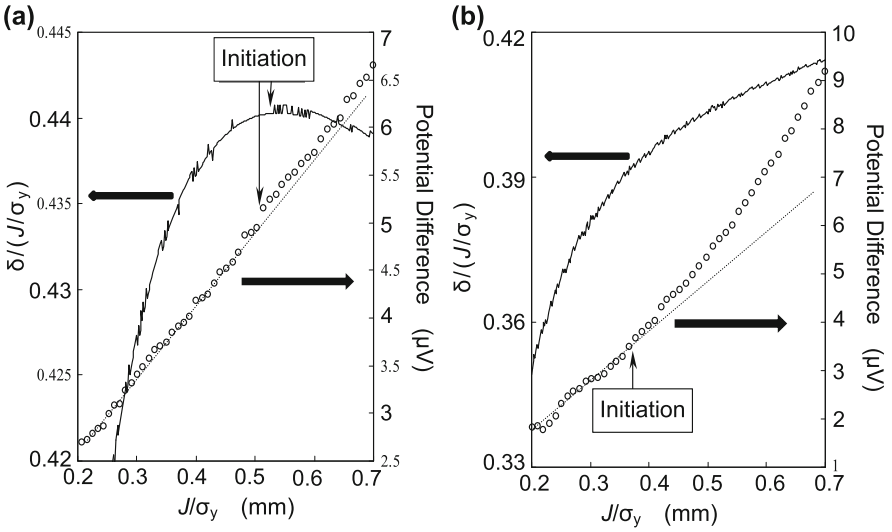

Fig. 6.12 The ratio of crack opening displacement, δ, to J/σ_y *vs.* increasing J/σ_y at a three-point bending test of notched specimen of a low carbon steel. Concurrently observed electric potential drop across the notch is also shown: (**a**) without and (**b**) with hydrogen precharging (Shimomura et al. [21])

result is shown in Fig. 6.12(a) [21] in which *J*-integral is normalized by the yield strength σ_y. The maximum on the $\delta/(J/\sigma_y)$ *vs.* J/σ_y curve corresponds to the appearance of a jog on the δ *vs.* J/σ_y curve. The crack initiation was confirmed by a simultaneous measurement of electric resistance across the ligament in front of the precrack, shown also in the figure. The crack initiation points detected by the two methods were quite consistent. The result reproduced a previous result by the method applied to a low-carbon low-alloyed steel of 6000 MPa in tensile strength [19].

Subsequently, the above method was applied to hydrogen effects on the crack initiation. The same steel used for Fig. 6.12(a) was hydrogen precharged to 0.82 mass ppm under a fairly mild fugacity using cathodic electrolysis in an aqueous solution of 3 % NaCl + 3 g/l NH_4SCN at a current density of 5 A/m^2 for 24 h. Promoted crack initiation by hydrogen was revealed by means of the electric resistance method as shown in Fig. 6.12(b), but $\delta/(J/\sigma_y)$ increased continuously with J/σ_y without showing a maximum. It implies that the opening of the precrack proceeds gradually without a large step-wise advance. The theory by Needleman and Tvergaard [20], described in Sect. 10.1.3, assumed that a discontinuous advance of the crack at a critical amount of void volume fraction is caused by the loss of stress-carrying capacity in the area adjacent to the crack. The observed rather gradual growth suggests that hydrogen coupled with strain-induced defects continuously and incrementally reduces the stress carrying capacity. The function of hydrogen originating in the enhanced creation of strain-induced vacancies is described in Sect. 10.5.

6.2.2 *Crack Growth*

(a) Growth rate ~ Gaseous hydrogen environment

Crack growth rate is important for kinetics of hydrogen embrittlement, and it has been examined mostly for Stage II in the three stages shown in Fig. 6.7. The steady crack growth rate at Stage II is little affected by the magnitude of stress intensity and is likely rate-controlled by some factors other than mechanical driving force.

The temperature dependence of the growth rate gives information on the controlling process. Temperature dependencies of the growth rate of AISI 4130 steel in 98 kPa hydrogen gas and at applied stress of 39 MPa · $m^{1/2}$ are opposite in sign according to temperature regions as shown in Fig. 6.13 [22]. Activation energies obtained from each Arrhenius relationship were 16 and −23 kJ/mol in Region 3 and Region 1, respectively. Similar opposite temperature dependencies of the Stage II crack growth rate were observed in 133 kPa dry hydrogen gas for AISI 4340 steel of 2082 MPa in tensile strength [12]. The activation energy of Stage II crack growth in Region 3 was 14.7 kJ/mol, close to 16 kJ/mol for AISI 4130 steel.

The crack growth in dry hydrogen gas proceeds with adsorption and following migration of hydrogen on the specimen surface. Williams and Nelson ascribed the rate-controlling process of the crack growth to adsorption of hydrogen on the steel surface taking into account the fractional coverage of initial adsorption sites [22]. Simmons et al. noticed that fractographic features at tests in hydrogen gas and in water are similar and deduced that surface reactions of water with steel controlled the crack growth rate in water [12].

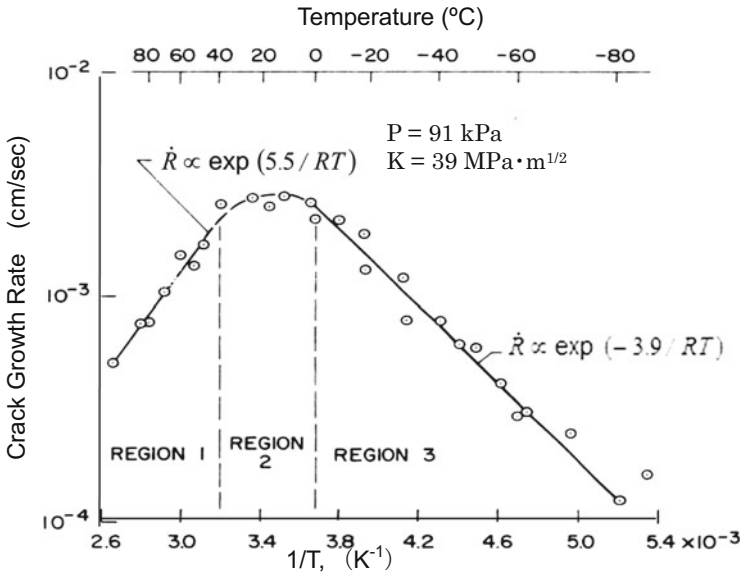

Fig. 6.13 Temperature dependence of the crack growth rate for AISI 4130 steel in low pressure hydrogen gas (Williams et al. [22])

The temperature dependence of Stage II crack growth rate varies by microstructures. For experiments with 18Ni maraging steels, tensile strength levels were controlled to 1330 MPa and 1720 MPa by tempering at 200 °C and 250 °C, respectively [23]. The temperature dependence of Stage II crack growth rate in dry hydrogen was similar to Fig. 6.13, but the slope in Region 1 was very steep. The transition temperatures from Region 1 to Region 3 in 133 kPa hydrogen gas were about 20 °C and −20 °C, respectively, for steels tempered at 250 °C and at 200 °C, respectively. Magnitudes of the crack growth rate at the transition temperature were also fairly different between the two steels, about 5×10^{-5} m/s and 5×10^{-6} m/s for tempering at 250 °C and 200 °C, respectively. The crack growth rate increased proportionately to $\sqrt{P_{H2}}$ in Region 3 with the activation energy of 18.4 kJ/mol irrespective of tempering temperatures and hydrogen gas pressures. Gangloff and Wei suggested that some reactions in a near surface region operated associated with hydrogen transport by diffusion, but the process controlling Region 1 was not definite [23].

Vehoff and Rothe found that the crack-tip opening angle (CTOA) α is constant during the stable crack growth at tensile loading of notched Fe-2.6%Si single crystals in low pressure hydrogen gas [24]. The value of α characterizes the amount of ductility accompanying crack growth. The fracture surface showed a very fine mixture of plastic shearing off and cleavage-like facets on a scale of 0.1 μm or less. The value of α was a function of temperature, hydrogen pressure or activities and crack growth rate. The temperature dependence of α in the intermediate temperature range 293 K $< T <$ 390 K showed an Arrhenius-type relation with an apparent activation energy of 49 kJ/mol. Vehoff and Rothe deduced that isolated microcracks were initiated along the crack front and that the embrittlement was related to the fractional hydrogen coverage of special sites right at the tip of a stressed crack with the binding energy of 49 kJ/mol [24].

Similar results were obtained with low cycle fatigue of nickel single crystals in electrolytes at different cathodic potentials. The fracture mode was a mixture of alternate slip and local brittle fracture [25]. The apparent binding energy obtained from the temperature dependence of CTOA was 32 kJ/mol.

(b) Crack growth rate ~ Internal hydrogen

Crack growth in gaseous hydrogen likely involves surface reactions, but the effects of internal hydrogen have been also examined. Three stages of crack growth rate of the type shown in Fig. 6.7 were observed at sustained-loading tests of hydrogen precharged AISI 4340 steels [13, 26]. Hydrogen precharging was conducted by cathodic electrolysis in poisoned 5 % H_2SO_4 aqueous solution at a current density of 20 A/m^2 and hydrogen was enclosed within the specimens by cadmium plating [26]. The crack growth in hydrogen-precharged specimens exhibited an incubation time and a transient stage before establishing the steady state Stage II. The growth rate at room temperature was at least one order of magnitude faster for specimens of 1620 MPa in yield strength by tempering at 230 °C than for 1340 MPa specimens by tempering at 450 °C. Stage II crack growth rates were also dependent on temperature with Arrhenius relations. A theoretical model for the crack growth rate was proposed assuming that the build-up of local

hydrogen concentration by diffusion to a critical value in the crack tip region triggered fracture there and induces the crack advance [26]. Using numerical values of parameters obtained from the literature, experiments and also as adjustable variable, crack growth rates were calculated to fit fairly well with the observed temperature dependence for 230 °C tempering. The estimated binding energies of hydrogen with the critical trap sites for the crack initiation were 75 kJ/mol and 27 kJ/mol for 230 °C and 450 °C tempering, respectively. Fractographic features were mixtures of IG and QC for specimens tempered at 230 °C. For tempering at 450 °C, alternate IG and MVC regions were assigned to intermittent slow and fast crack growth. Details of fractographic features are described in Sect. 7.1(e).

In the model proposed by Gerberich et al. [26], crucial assumptions are (i) the fracture stress decreasing in proportion to hydrogen concentration, and (ii) high local hydrogen concentrations due to both the dilatational stress field and trap-binding effects. Plastic constraint was also taken into account for computing the triaxial stress at the critical site. Critical trap sites to cause sequential fracture were assigned from fractographic observations to martensite lath boundaries intersecting the prior austenite grain boundaries for 230 °C tempering and to oxysulfides located at the edge of plastic zone for tempering at 450 °C. However, the critical hydrogen concentrations that the model estimated at the trap sites were very high, more than 10^6 times of hydrogen in solution. The problems are further described in Sect. 8.1 (a) about fractographic features and in Sect. 9.3 about the mechanism.

(c) Crack growth resistance

The resistance against rack growth rate is a direct measure of intrinsic degradation of materials. Crack growth resistance curve (R-curve) plots the total energy dissipation rate as a function of the crack length in slow stable crack growth. The total energy dissipation rate is expressed in terms of the J-integral in the elastic–plastic regime. Figure 6.14 [27] compares R-curves of notched specimens of low

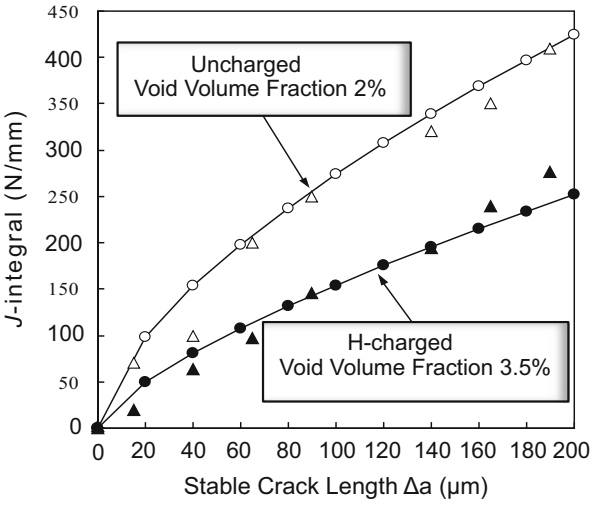

Fig. 6.14 R-curves of low carbon ferrite-pearlite steel with and without hydrogen precharging. ○, ● : observed values; Δ, ▲ : calculated values using a finite element method (Nagumo et al. [27])

carbon ferrite-pearlite steel subjected to three-point bending tests with and without hydrogen precharging. Hydrogen charging was conducted in a mild condition by cathodic electrolysis in 3 % NaCl + 3 g/*l* NH_4SCN aqueous solution at a current density of 5 A/m^2 for 24 h. A substantial decrease in the crack growth resistance appeared for hydrogen-charged specimens. The marks Δ and ▲ in the figure for specimens without and with hydrogen precharging, respectively, denote calculated *J*-integral values from the stress and strain fields near the crack. A constitutive relation for porous materials was used for the calculation, and the decrease in the *J*-integral by hydrogen was ascribed to an increase in nucleation void densities. The method of modelling *R*-curve in Fig. 6.14 is described in Sect. 10.5.3. *R*-curve is closely related to strain-induced lattice defects and analyses of microscopic origins are described in Sect. 10.5.2.

Effects of hydrogen on *R*-curve were also shown for disc-shaped compact tension specimens of 21Cr-6Ni-9Mn austenitic stainless steel [28]. Hydrogen was thermally precharged to 210–230 mass ppm in high pressure hydrogen gas. The fracture initiation toughness J_Q was defined as the *J* value at the intersection of the 0.2 mm offset blunting line with the *R*-curve. Alternatively, initial damage at the precrack tip was detected as a subtle deviation from linearity of the COD *vs*. crack length measured using the direct current potential difference according to ASTM E1737. The deviation point was denoted as J_i and J_Q according to the choice of the initial blunting line. Hydrogen reduced both J_i and J_Q by more than 80 % from the values for hydrogen-free specimens. Crack growth resistance denoted by d*J*/d*a* also decreased nearly 50 % by hydrogen. Nibur et al. carefully examined deformation microstructures that exhibited enhanced strain localization. The features are described in Sect. 7.3.1.

The *R*-curve is strongly dependent on microstructures of steels. It was revealed for ferrite-pearlite steels that carbides precipitated along grain boundaries acted as barriers against slip extension across grain boundaries and affect *R*-curves prominently [29]. The functions of the slip constraint in *R*-curve for that case are described in Sect. 10.5.2 about the strain-induced creation of vacancies.

6.3 Fatigue

Fatigue failure is the most common type of failure of metallic structural components in practical services. Not only under high pressure hydrogen gas environments, hydrogen comes from humid or corrosive environments, during cathodic protection of off-shore structures, or at electroplating, and plays a crucial role in fatigue failure. Corrosion fatigue is often caused by hydrogen produced by corrosion reactions on the metal surface.

Fatigue properties of materials are commonly expressed in terms of fatigue life and fatigue limit determined from the plot of the stress amplitude *vs*. the number of cycles to failure (*S-N* curve). The fatigue limit $\Delta\sigma_c$ and the threshold stress intensity range for no detectable crack growth ΔK_{th} are design parameters for the safety

against fatigue failure [30]. Fatigue failure proceeds through the crack nucleation and growth. Measurements of fatigue-crack growth in laboratories are conducted commonly using notched specimens. Fatigue tests consume a substantial time for one run, and hydrogen contents in specimens are often not constant during a test-run due to the entry and loss of hydrogen and/or internal changes of materials.

Fatigue failure is affected by many factors and their effects are not similar among different expressions of fatigue properties. Early works for hydrogen effects on metal fatigue were reviewed by Gerberich with respect to different approaches such as total life, threshold and crack growth [31].

(a) *S-N* curve

Hydrogen generally reduces fatigue life and fatigue limit. Figure 6.15 [32] plots tension-compression fatigue test data of two lots of surface-hardened 0.36C-Cr-Mo martensitic steel with/without hydrogen. Hydrogen was initially charged by immersing specimens in 20 % NH_4SCN aqueous solution at 50 °C, and hydrogen contents were controlled to 10, 0.8 and 0.3 mass ppm by partial degassing at room temperature. Fatigue specimens contained a small hole of 100 μm in both diameter and depth on the specimen surface as the crack starter. Fatigue tests were conducted at a stress ratio R ($= \sigma_{max}/\sigma_{min}$) of -1 and with different frequencies up to 1000 Hz. Hydrogen was recharged to specimens every 8×10^6 fatigue cycles so as to keep the same content during the test. The control of hydrogen content was by partial degassing, and the reductions in fatigue life and fatigue limit by hydrogen were reversible against the entry of hydrogen. A small amount, ~ 0.3 mass ppm, of hydrogen remaineded in as-heat-treated specimens, and thermal desorption analysis

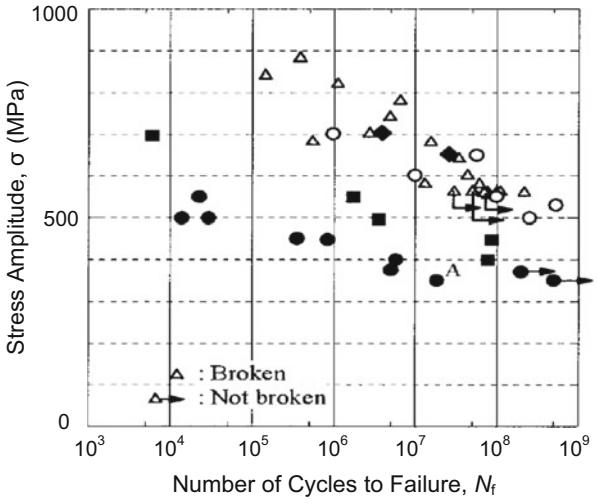

Fig. 6.15 Effects of hydrogen on *S-N* diagram of two lots of SCN 435 steel. Open marks, as-heat-treated (0.3 ppm H); Solid marks, H-charged. Initial hydrogen contents are controlled by partially degassing at room temperature after hydrogen charging: ● (10 ppm), ■ (100 h after hydrogen charging, 0.8 ppm), ♦ (4300 h after hydrogen charging, 0.3 ppm) (Murakami et al. [32])

(TDA) showed a small peak at 300 °C indicating strongly trapped non-diffusive nature of residual hydrogen as described in Sect. 2.1.2. On the other hand, artificially charged hydrogen diffused out at room temperature exposure and the thermal desorption ceased by 300 °C. The observations imply that the degradation is caused by diffusive hydrogen. Murakami et al. revealed the fatigue-crack initiation from non-metallic inclusions [32]. Non-metallic inclusions are possible trap sites of non-diffusive hydrogen, but non-diffusive hydrogen is generally immune to degradation. Alternatively, diffusive hydrogen might interact with non-metallic inclusions and/or with plastic deformation around inclusions, but the changes of trapped states during fatigue cycles were not examined.

Hydrogen effects to decrease fatigue life and fatigue limit at rotational bending tests are shown in Fig. 6.16 [33] for unnotched round bar specimens. The steel was a high strength Si-Cr martensitic steel hydrogen precharged under a fairly mild condition by cathodic electrolysis in a 3 % $NaCl + 3gl^{-1}$ NH_4SCN aqueous solution at a current density of 7.5 A/m^2. Lattice defects produced during fatigue were detected by introducing hydrogen as the tracer of defects into fatigued specimens after removing precharged hydrogen at room temperature. The tracer hydrogen exhibited a single peak at about 120 °C on TDA, indicating weakly trapped states. The amounts of the tracer-hydrogen in fatigue-fractured specimens at two applied stress levels are shown in Fig. 6.17 [33]. The stress amplitude of 580 MPa was close to the fatigue limit. The amounts of the tracer hydrogen were larger in hydrogen-precharged specimens than in uncharged ones in spite of shorter fatigue cycles for hydrogen-precharged specimens. The results suggest that the promoted failure by hydrogen is due to the enhanced creation of defects during fatigue cycles. Vacancy-type nature of defects created during fatigue cycles is described in Sect. 7.3.1.

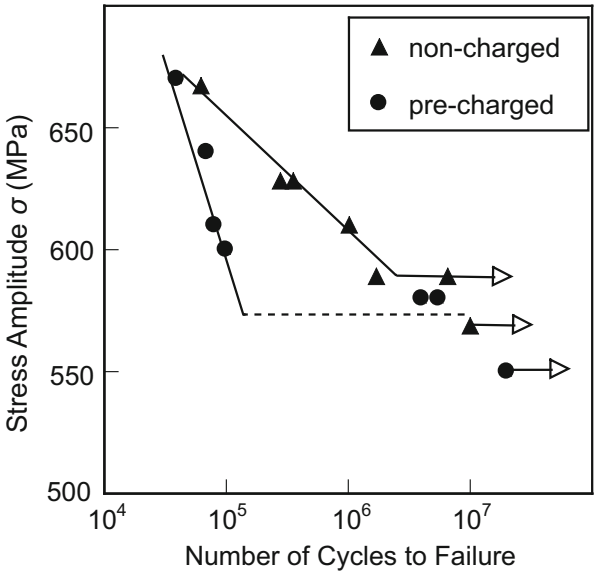

Fig. 6.16 *S-N* diagrams at rotational bending fatigue for Si-Cr martensitic steel with and without hydrogen precharging. The arrows indicate no failure (Nagumo et al. [33])

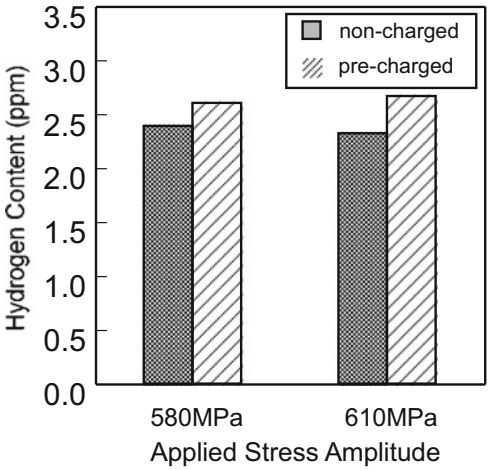

Fig. 6.17 The amounts of tracer-hydrogen in Si-Cr steel specimens fatigue-fractured at two applied stress amplitudes with and without hydrogen precharging. Fatigue cycles applied to the non-charged and pre-charged specimens were respectively 6×10^6 and 5.5×10^6 at the stress amplitude of 580 MPa, and 2×10^5 and 8×10^4 at the stress amplitude of 610 MPa (Nagumo et al. [33])

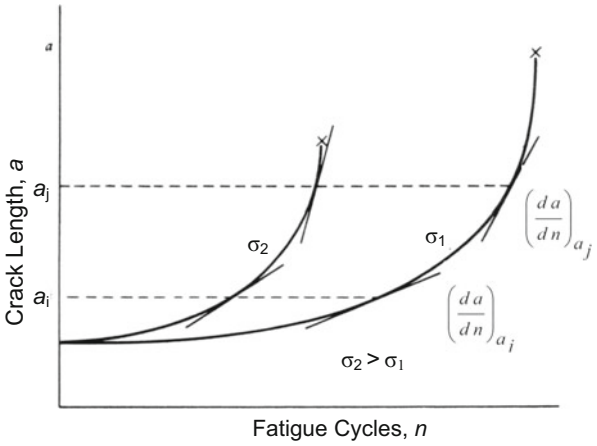

Fig. 6.18 Schematic illustration of applied stress dependence of fatigue crack growth (Hertzberg [30])

(b) Fatigue-crack growth

The growth of a fatigue-crack starting from the surface notch is schematically shown in Fig. 6.18 [30] against fatigue cycles for two applied stresses. The crack growth rate is computed from the observed crack length record. It should be noticed, particularly at the regime of crack growth rates as low as 1×10^{-9} m/cycle, that the computed growth rate does not necessarily mean the actual crack advance at every cycle. Environments often complicate the morphology of the notch root, and the effects of corrosion or oxidation overlap hydrogen embrittlement.

Environmental effects on fatigue crack growth of high strength steels are complicated according to ΔK level and stress ratio. Accelerated fatigue crack growth in hydrogen gas compared to that in air was reported for 2¼ Cr-1Mo steels at two

growth rate regimes, *i.e.* at near threshold levels and at higher growth rates typically $>10^{-8}$ m/cycle above a critical $K_{\max}$ value [34]. The hydrogen effect in the latter regime appeared at frequencies below a critical value (*e.g.* 5 Hz at the stress ratio of 0.05) associated with a fracture mode change to predominately intergranular cracking, consistently with general features of hydrogen embrittlement.

On the other hand, at near threshold levels below 10^{-9} m/cycle, the accelerated growth rate in dry hydrogen compared to moist air appeared only at low load ratios [34]. Suresh et al. ascribed the influence of environment on near-threshold fatigue crack growth to the oxide-induced crack closure mechanism. An earlier contact between the facture surfaces during the closure portion raises the closure load and reduces ΔK_{eff} as

$$\Delta K_{eff} = K_{max} - K_{cl}, \tag{6.4}$$

where K_{cl} is the stress intensity to close the crack. Thus reduced ΔK_{eff} decelerates crack growth rates at low load ratios. The deceleration of fatigue-crack growth due to crack closure is prominent when the crack opening is small at low ΔK levels and low stress ratios in corrosive environments. The magnitude of mechanical wedging action is a function of the thickness and location of the debris [35]. Suresh et al. noted that pulsating crack-tip opening displacements were of a size comparable to fracture surface roughness and the thickness of corrosion debris within the crack [34].

The initiation and the early stage growth of fatigue crack, especially in the range of very small ΔK under corrosive environments, have been extensively studied [31, 36]. Fatigue crack growth rates of high strength steels under the same applied stress intensity increased in 3 % NaCl aqueous solution and water compared to those in air. The increase was much higher for short than for long cracks [31]. An expression of short crack effects is to use ΔK_{eff} by adding an effective crack length l_0 to the actual crack length l [36, 37], *i.e.*

$$\Delta K_{eff} = A\,\Delta\sigma\sqrt{\pi\,(l + l_0)}, \tag{6.5}$$

where A is the elastic stress concentration factor and $\Delta\sigma$ is the applied nominal stress range. The magnitude of ΔK_{eff} is larger than the apparent ΔK, and the contribution of l_0 to ΔK_{eff} is significant when l is small. Environmental effects are ascribed to large l_0 in the presence of corrosive environment. However, the physical meaning of l_0 is not definite while an intrinsic defect size such as a microfracture process zone size has been proposed.

The fatigue crack growth rate is often expressed by Paris' law as a function of ΔK,

$$\frac{da}{dN} = A\Delta K^m, \tag{6.6}$$

where A and m are constants that vary with material, environment and testing conditions [30]. Fatigue tests in high pressure hydrogen gas of Ni-Cr-Mo

Table 6.1 Fatigue crack growth parameters in Eq. (6.6) for as-quenched and tempered martensitic steels in Ar and hydrogen environments

Steel	Quenched (TS:1344 MPa)			Quenched-Tempered (TS: 1274 MPA		
Atmosphere	Ar	1.1 MPa H_2	4 MPa H_2	Ar	1.1 MPa H_2	4 MPa H_2
m	4.1	6.5	7.1	4.7	12.1	15.6
K_Q (MPa $m^{1/2}$)	59	23	17	72	27	21

Fukuyama et al. [38]. Reprinted with permission from The Society of Materials Science, Japan

martensitic steel subjected to two types of heat-treatment, *i.e.* as quenched and quenched-tempered, showed increased crack growth rates with increasing hydrogen gas pressure at a given ΔK [38]. The growth rate at a given ΔK was much higher for the as-quenched martensite than for the tempered one, but the susceptibility of the growth rate to hydrogen expressed in terms of m-value in Paris' law was higher for the tempered martensite than for the as-quenched one as shown in Table 6.1 [38]. The fatigue tests were conducted using DCB specimens at $R = 0.1$ and a sinusoidal frequency of 5 Hz. The as-quenched martensite exhibited significant hydrogen effects at small ΔK near the threshold, while the effects were almost insignificant for tempered martensite at 573 K. The reason is not definite. Closure effects due to oxides or debris are not likely since all the tests were conducted under dry environments. The susceptibility to hydrogen embrittlement in terms of fracture toughness K_Q is included in Table 6.1, and the reductions by hydrogen in terms of the ratio to the fracture toughness in argon gas were of similar levels for the two heat-treatments.

Enhanced crack growth rate by internal hydrogen at near-threshold region was deduced by Esaklul et al. separating from any crack closure effects [39]. The steel was AISI 4340 steel of 1800 MPa in tensile strength, and hydrogen was precharged under a fairly high fugacity by cathodic electrolysis in poisoned 5 % H_2SO_4 at a current density of 20 A/m^2 followed by cadmium plating. Fatigue tests were conducted using CT specimens at $R = 0.1$ and 30 Hz. Plots of log da/dN *vs.* nominal ΔK showed enhanced crack growth rates by hydrogen at ΔK above 7 MPa-$m^{1/2}$ or in da/dN above 5×10^{-9} m/cycle. However, crack growth rates were almost identical for hydrogen-charged and uncharged specimens in the lower ΔK range. Fractographic features showed oxide buildup, and geometrical asperities for hydrogen-charged specimens and the load *vs.* crack-opening-displacement curves exhibited closure of the crack surface. Then, the nominal ΔK was converted to ΔK_{eff} in Eq. (6.5) using the estimated contact area and contact point on the observed fracture surface. Then, the plots of log da/dN against ΔK_{eff} revealed hydrogen-enhanced crack growth rates even in the ΔK_{eff} range below 5 MPa-$m^{1/2}$ or in da/dN below 1×10^{-9} m/cycle.

Hydrogen generally promotes the crack initiation and growth in fatigue, but unexpected "decrease", rather than increase, in fatigue crack growth rates was reported for a tension-compression fatigue test of Type 304 and Type 316 L austenitic stainless steels containing more than about 70 wt. ppm hydrogen [40]. The specimens were round bars of 7 mm in diameter, and hydrogen was

precharged in a high pressure hydrogen gas at high temperatures. A small hole, 100 μm both in depth and diameter, was drilled on the surface after hydrogen charging as the starter of fatigue crack. Fatigue tests were conducted at 1 Hz and a stress ratio of −1, and the advancing crack length was measured on the surface using a replica method.

On the contrary, a stress-controlled fatigue test using compact tension specimens of Type 304 and Type 316 L containing 70 ppm of hydrogen showed accelerated fatigue crack growth by hydrogen more pronouncedly for Type 304 than for Type 316 L [41]. The tests were conducted at the stress ratio of 0.1 and the frequency of 1, 0.1 and 0.01 Hz. Also, cyclic-pressurization fatigue tests using tubular specimens without a notch in high pressure hydrogen gas showed a decrease in the fatigue life for Type 304 steel [42]. The maximum and the lowest internal hydrogen gas pressures were 88 MPa and 0 MPa, respectively, and the cycle time was 20s per cycle. Type 316 L showed no degradation in this type of tests even for tubular specimens notched on the internal surface. A precipitation-hardened austenitic stainless steel A285 and a low alloy Si-Cr-Mo high strength steel showed a substantial degradation in fatigue life by hydrogen [42]. The characteristics of hydrogen embrittlement of austenitic steels are described in Sect. 8.4.

(c) High cycle fatigue near threshold

Fatigue crack growth behaviors near the threshold stress intensity range are of practical importance for structural components under long-term service. Threshold, below which the crack growth rate becomes diminishingly small, was not found for ultrasonic tension-compression fatigue tests near the ΔK_{th} ranges of mild steel, Type 304 stainless steel and copper in 3.5 % NaCl aqueous solution, but a distinct threshold existed in non-corrosive silicon oil [43]. The fracture mode of samples fatigued in corrosive environment changed from ductile transgranular to intergranular fracture.

Involvement of a very small amount of hydrogen in extremely high cycle fatigue limits was presented by Murakami et al. [44] for a surface-hardened Cr-Mo steel quenched and tempered in a reductive atmosphere (QT) or in a vacuum (VQ). Hydrogen entered into specimens during the fabrication process and the concentrations were 0.7–0.9 and 0.01 mass ppm for QT and VQ, respectively. Fatigue tests were tension-compression at $R = -1$ with cyclic frequency of 20–80 Hz. For extremely high cycle fatigue in the regime of $N > 10^7$, the *S-N* plots showed a substantial scatter but fatigue lives and fatigue limit were lower for QT than VQ. Murakami et al. pointed out the importance of non-metallic inclusions. Crack initiation sites were subsurface non-metallic inclusions located at centers of fish-eye associated with optically dark area (ODA) characterized by rough and irregular surface morphology. The size of ODA in QT was about twice as large as that of non-metallic inclusions and was larger than ODA in VQ. Secondary ion mass spectroscopy detected hydrogen at near non-metallic inclusions in QT but not in VQ. Murakami et al. deduced that hydrogen assists the formation of ODA and determines fatigue lives at low stress levels near the fatigue limit [44]. At an extremely slow crack growth stage of 1×10^{-10} m/cycle, more than thousands of

cycles were applied in order that a detectable crack advance took place. Effects of some structural damages might be expected.

6.4 Delayed Fracture

Eventual failure in a long-term use under mild corrosive environments is a crucial problem for the structural components of high strength steels. Periods of service until fracture range to years. For laboratory tests, delayed fracture characteristics are expressed by the applied stress *vs.* time to fracture diagram similar to the *S-N* curve for fatigue tests. Accordingly, an alternate terminology for sustained-loading delayed fracture is "static fatigue". Fracture mechanics test under sustained loading is a type of delayed fracture. The threshold stress intensity for the crack initiation K_{TH} described in Sect. 6.2.1 for fracture mechanics tests corresponds to the lower limit of the applied stress below which delayed fracture does not occur, but notches are not requisite to induce delayed fracture. Delayed fracture diagrams vary by testing temperature, environment or hydrogen concentration, and specimen geometry. A long exposure time to fracture in practical services inevitably necessitates some accelerated tests in laboratories. The correspondence between practical and laboratory test results is a matter that needs careful examination.

6.4.1 Factors Affecting Delayed Fracture

Early works intended to disclose the role of hydrogen in delayed fracture. Figure 6.19 [45] for AISI 4340 steel of 1600 MPa in tensile strength might be historically the first diagram obtained by laboratory tests under constant-stress tensile loading. The specimens were circumferentially notched bars, and hydrogen was precharged under a fairly high fugacity by cathodic electrolysis in 4 % H_2SO_4 at a current density of 30 A/m^2. Hydrogen was enclosed in specimens by cadmium-electroplating, and the Cd-plated specimens were then baked at 150 °C (=300 °F) to homogenize the distribution of hydrogen. Partial degassing took place during baking, but hydrogen concentrations were not measured. Instead, baking times at 150 °C were used as the parameter of hydrogen concentration. As-received specimens contained about 1.5 mass ppm of hydrogen exceeding electrolytically introduced hydrogen, but the as-received hydrogen was immune to the embrittlement. It suggests that apparent hydrogen concentrations do not always serve as a measure for causing degradation.

Another diagram for the effects of hydrogen concentrations on delayed fracture is the plot of diffusive hydrogen concentrations *vs.* the time to fracture under a given applied stress [46, 47]. For martensitic steels, hydrogen was precharged without [46] or with [47] cadmium plating and most fracture took place within 24 h. Hydrogen concentrations were measured by means of thermal desorption

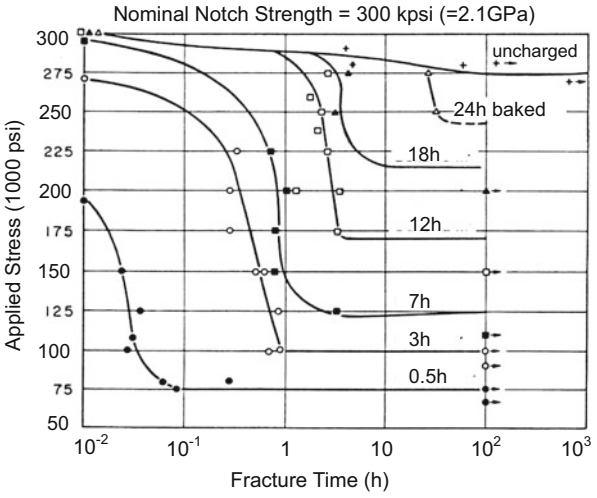

Fig. 6.19 Delayed fracture diagram of AISI 4340 steel. Hydrogen-charged specimens are Cd-plated and baked at 150 °C for various periods (Johnson et al. [45])

analysis, and the amounts hydrogen desorbed below 500 K were employed as the amount of diffusive hydrogen. Delayed fracture is sensitive to specimen geometries. The notch radius on specimens used for Fig. 6.19 was 25 μm, but the notch sharpness affects delayed fracture diagrams [45] in a similar form as the effects of baking times shown in Fig. 6.19. Delayed fracture test methods using specimens without an artificial notch were also presented for the assessment of stress corrosion cracking of prestressing steel bars [48].

The susceptibility to delayed fracture is generally higher for steels of higher strength levels. Figure 6.20 [49] compiles threshold stresses of various commercial steels subjected to delayed fracture tests in water for 100 h. The threshold stress turns to decrease for steels of the tensile strength higher than 1200 MPa, which corresponds to the strength level of high strength fasteners that exhibit delayed fracture in service under atmospheric environments. It is to be noticed that the critical tensile strength above which the threshold stress turns to decrease differs by steel types. Maraging steels have higher resistance than low-alloyed steels, and the mechanism is an important subject for designs of hydrogen-resistant steels. Testing temperature also substantially affects the time to fracture. For sustained tensile-loading delayed fracture tests in water for a martensitic steel of 1510 MPa in tensile strength, elevation of water temperature from 25 °C to 80 °C reduced the time to fracture more than one order of magnitude [49] .

For fracture mechanics tests, the critical stress intensity K_{TH} below which no cracking occurs is affected by stress states operating on the specimen. The stress state in the vicinity of crack-tip changes from plane strain to plane stress as the thickness and/or the yield strength of the specimen decreases. Gerberich and Chen showed that the transition from a plane strain to a plane stress state increases K_{TH} [50], but conceivable mechanisms of the effect of stress states are not simple. Triaxial stress enhances the buildup of local hydrogen concentration, but it also promotes the void nucleation and growth rates as microstructural effects.

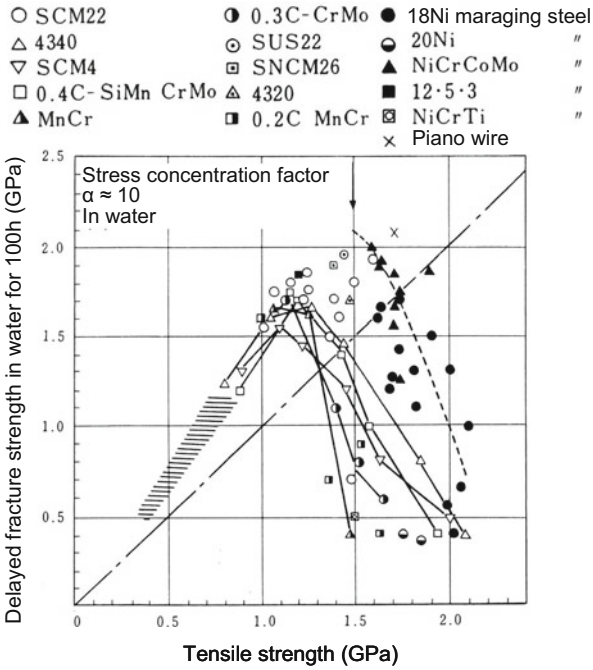

Fig. 6.20 Threshold stresses at 100 h for delayed fracture of various high strength steels in water (Yamamoto et al. [49])

6.4.2 Incubation Period

The initiation of an incipient crack and its growth take place substantially prior to the onset of final fracture at delayed fracture tests. The initiation and discontinuous growth were detected by means of electric resistance techniques [45, 50]. The incubation period before the crack initiation was prolonged by decreasing hydrogen concentration, but it was almost independent of the applied stress for a given hydrogen concentration [51]. The incubation period covers a major part of the time to fracture at high applied stresses. Assuming a diffusion-controlled process in the incubation period, Steigerwald et al. obtained the activation energy of 38 kJ/mol from an Arrhenius relationship for the logarithm of the ratio of the incubation time to the absolute temperature [51]. The value is fairly higher than reported activation energies for hydrogen diffusion in iron and steels and some other controlling processes are not ruled out. A noteworthy result was that the true fracture stress, *i.e*. applied stress divided by the uncracked area determined on the fracture surface, was constant over a wide range of applied stress and of hydrogen concentration. It suggests that the fracture stress in the central portion of specimens is irrelevant to hydrogen concentrations. If the true fracture stress represented the critical degradation of the material during the delayed fracture test, the observation might suggest that hydrogen functions in some kinetics during the incubation period rather than at the final fracture stage before reacing a critical state.

Events that happen in the incubation period of delayed fracture tests were detected by means of acoustic emission (AE) technique for high strength steels of

1300 MPa in tensile strength [52]. The delayed fracture tests were conducted using V-notched specimens subjected to a constant load cantilever bending in 0.1 N HCl solution. Acoustic emissions were observed in the incubation period prior to the onset of the crack initiation that was detected by a concurrently conducted electric resistance measurement. The number of AE signals increased with time and their wave forms in the incubation period and the crack growth stage are compared in Fig. 6.21 [52]. The wave form in the incubation period was packet-like similar to that emitted associated with plastic deformation, while that in the crack growth stage was irregular with higher amplitudes.

Interactions of hydrogen with strain-induced lattice defects are possible functions of hydrogen in the incubation period. Mechanistic behaviors in delayed fracture tests are essentially the same as stress relaxation and creep that involve plastic deformation as described in Sect. 5.3. Hydrogen enhanced stress relaxation shown in Fig. 5.5 for a 0.37%C-0.6%Si-1.0%Mo-0.5%Cr-0.54 V martensitic steel indicates that the precipitation of fine VC reduces both the stress relaxation rate and its enhancement by hydrogen. Delayed fracture test results of the same steel are shown in Fig. 6.22 [53]. Two tempering temperatures of 550 °C and 650 °C were

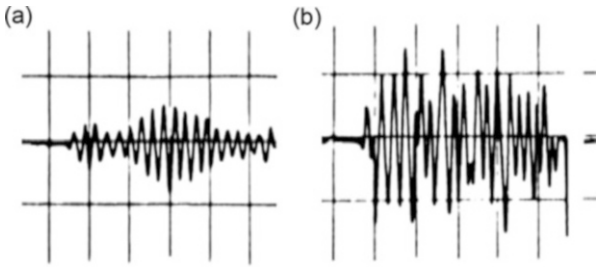

Fig. 6.21 Wave forms of acoustic emission generated during delayed fracture tests of high strength martensitic steel. (**a**) Incubation time, (**b**) During crack extension (Nagumo [52])

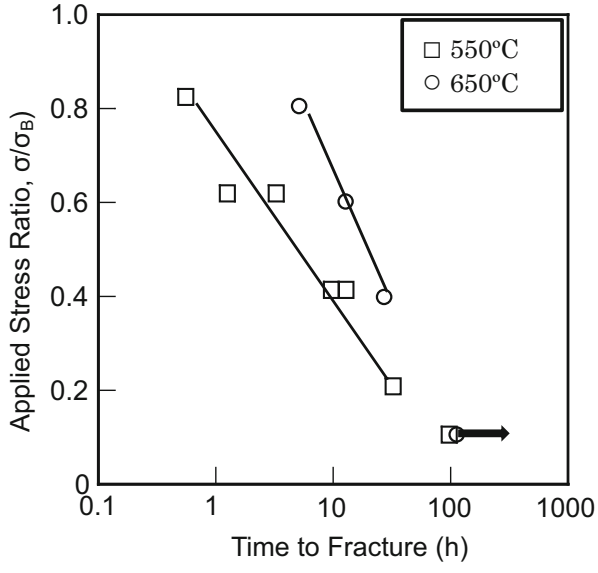

Fig. 6.22 Delayed fracture diagrams for medium carbon Mo-V martensitic steels tempered at 550 °C and 650 °C. The arrow indicates unfailed specimens (Nagumo et al. [53])

employed to give the same tensile strength of 1470 MPa for both with and without VC precipitation. Sustained loading tests were conducted at room temperature using flat specimens hydrogen-precharged under a mild hydrogen fugacity by cathodic electrolysis in a 3 % $NaCl + 3gl^{-1}$ NH_4SCN solution at a current density of 5 A/m^2. Precipitation of fine VC brought about a substantial improvement of the time to fracture. The correspondence between the stress relaxation rates and hydrogen effects implies involvements of plasticity and associated hydrogen effects in delayed fracture.

A further issue is microstructural alterations associated with plastic deformation in the incubation period. A common notion so far assumed for the origin of delayed fracture is buildup of hydrogen concentration to some critical values, and it has been widely adopted as the mechanism of delayed fracture. However, reported data of hydrogen concentration in structural components exposed to environments for long terms are few. Figure 6.23 [54] shows hydrogen contents in high strength steel specimens exposed to atmospheric environments at various sites in Japan for four years. The specimens were 1500 MPa in tensile strength and flat plates of 3 mm in thickness were U-shape bent. Hydrogen contents were measured by means of TDA as the amounts of hydrogen desorbed below 200 °C at which the desorption almost ceased. Hydrogen contents increased with time, as expected, in initial six months, but tended to decrease to a constant level on further exposure. Data showed a substantial scatter, but systematic effects of local climates were not discernible. The facts are against the common notion and imply that hydrogen contents are not always the decisive factor to cause delayed fracture.

The enhanced creation of strain-induced vacancies by hydrogen is described in Sect. 3.2.3(b). Changes of hydrogen contents during immersion in 20 % NH_4SCN

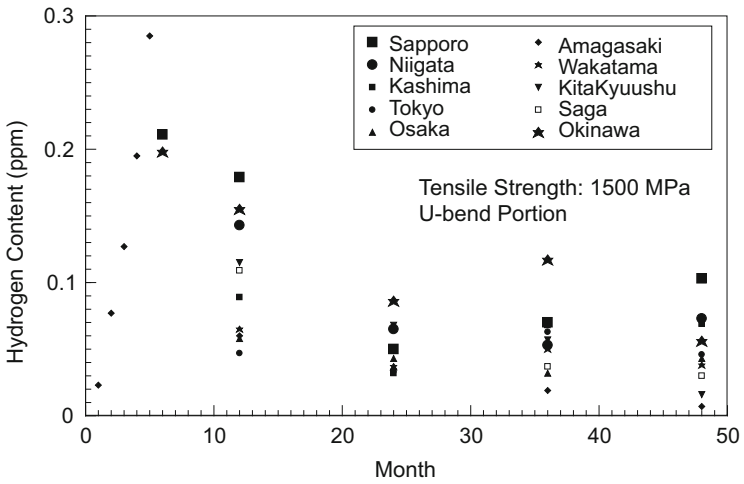

Fig. 6.23 Hydrogen contents in U-bend loaded high strength steel sheets of 1500 MPa in tensile strength after exposure at various sites in Japan (Kushida [54], Reprinted with permission from The Iron & Steel Inst. Japan)

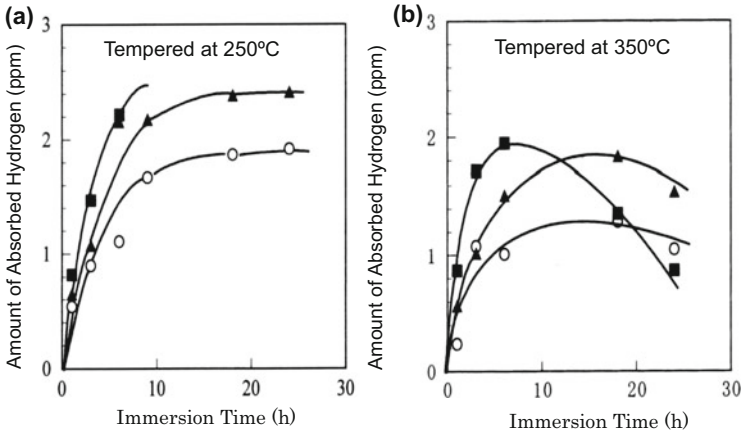

Fig. 6.24 Amounts of absorbed hydrogen in medium carbon tempered martensitic steels during immersion in 20 % NH_4SCN aqueous solution at 50 °C. ○, unloaded; ▲, prestressed to 80 % of the tensile strength; ■, concurrently loaded to 80 % of the tensile strength. (**a**) tempered at 250 °C, (**b**) tempered at 350 °C (Nagumo et al. [55])

aqueous solution at 50 °C are shown in Fig. 6.24(a) [55] for 0.33 % C martensitic steel bars of 5 mm in diameter. The order of the increase in hydrogen content among three conditions, *i.e.* (○) unstressed, (▲) prestressed at 80 % of the tensile strength and (■) under sustained-loading at 80 % of the tensile strength, corresponds to the order of strain-induced creation of lattice defects and its enhancement by hydrogen. However, unexpectedly, the increase in the hydrogen content was not monotonic in the steel tempered at 350 °C as shown in Fig. 6.24(b). The hydrogen content turned to decrease with the increasing loading time. The TDA profile of absorbed hydrogen for each condition showed a single broad peak between 50 °C and 200 °C. Comparisons of TDA profiles for the three conditions revealed that the higher temperature side of the TDA peak was associated with the increase in hydrogen contents. It implies, as described in Sect. 2.1.2, that traps with high binding energies with hydrogen are formed during the immersion. Alterations of strain-induced defects during delayed fracture tests have been discussed with respect clustering of vacancies [55].

The initial increase and subsequent decrease in hydrogen contents during sustained-loading delayed fracture tests were reproduced for another martensitic steel in a separate study [56]. Hydrogen contents represent densities of lattice defects that trap hydrogen, but hydrogen contents in Fig. 6.24 are the amount of hydrogen that entered into specimen through electrochemical reactions on the metal surface during the tets. Then, alteration in lattice defects during delayed fracture tests was separately evaluated in terms of tracer-hydrogen which was re-introduced into specimens after testing. Tracer-hydrogen was introduced into specimens interrupting loading and degassing at 30 °C for 168 h at the unloaded state. Figure 6.25 [56] shows the amounts of tracer-hydrogen introduced to fine-grained 0.32 % C martensitic steel specimens subjected to sustained-loading in 20 %

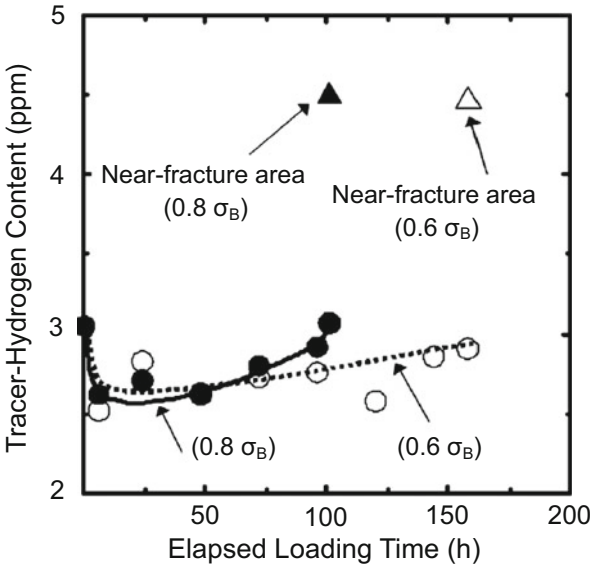

Fig. 6.25 Amounts of tracer-hydrogen introduced to martensitic steel bar specimens subjected to sustained-loading at 0.6 or 0.8 of the tensile strength in 20 % NH_4SCN aqueous solution at 50 °C. Δ and ▲ denote fractured specimens (Doshida et al. [56]. Reprinted with permission from The Iron & Steel Inst. Japan)

NH_4SCN aqueous solution at 50 °C. The applied stress was 60 % or 80 % of the tensile strength and both levels were apparently within the elastic range.

The amount of tracer-hydrogen, *i.e.* hydrogen absorption capacity, initially decreased but then gradually increased with increasing loading time. In fractured specimens, the portions near the fracture surface showed substantially high tracer-hydrogen contents as indicated by Δ and ▲ marks. The high values are due to concentrated strain near the fracture surface, and the findings are consistent with the strain-induced creation of vacancies and its concern with fracture. The initial decrease may be due to reconfigurations of dislocations associated with hydrogen-entry and loading. A similar initial decrease followed by a gradual increase in tracer-hydrogen content was also observed for a rotational bending fatigue test of high strength steel [33]. Alterations of TDA profiles with increasing sustained-loading time [55] are consistent with the formation of vacancy clusters as described in Sects. 2.1.2 and 3.2. Positron annihilation spectroscopy is a more direct method to identify vacancies. Concurrently conducted positron probe microanalysis (PPMA) revealed the formation of a high density of vacancy clusters near the fracture surface corresponding to TDA results [56].

6.4.3 Effects of Environmental Variations

Structural components tolerate more or less variations of applied stress and environmental condition even in apparently stationary usages. Alternating hydrogen entry due to daily changes of humidity in ambient atmosphere is demonstrated in

Fig. 2.3 in Sect. 2.1.1. Delayed fracture is normally assigned as the fracture under static loading, but the effects of mechanical and electrochemical variations must be considered.

(a) Stress variations

Superposition of small amplitude stress oscillation on sustained-loading promotes the macroscopic crack initiation and decreases the lower limit stress in delayed fracture tests [57]. The used material was Ni-Cr-Mo steel of 1800 MPa in tensile strength and sinusoidal oscillation of 15 or 400 cpm was superposed on U-notched static bending at various constant stresses. The promotion of the crack initiation by the superposed oscillating stress was prominent when water was dropped at the U-notch. The degradation appeared for stress amplitude as low as 50 MPa at the constant stress of 1260 MPa, and the degradation was more prominent with higher stress amplitudes and oscillating frequencies. Results for various steels are shown in Fig. 6.26 [58] at the oscillating frequency of 15 cpm and the stress amplitude of 50 MPa. Superposition of oscillating stress on sustained-loading delayed fracture tests may induce interactive functions of hydrogen operating alternately in delayed fracture and fatigue.

For experiments shown in Fig. 6.26, the maximum applied stress was raised by the superposition of the oscillatory stress. In order to separate effects of the cyclic variation and the level of the applied stress, another method to keep the maximum stress constant during the test was used. For sustained–loading delayed fracture tests of martensitic steel, the load was cyclically reduced by up to 10 % at a frequency of 5 or 10 cpm [59]. The steel was 1300 MPa in tensile strength and specimens of 5 or 7 mm in diameter were immersed in 20 % NH_4SCN aqueous

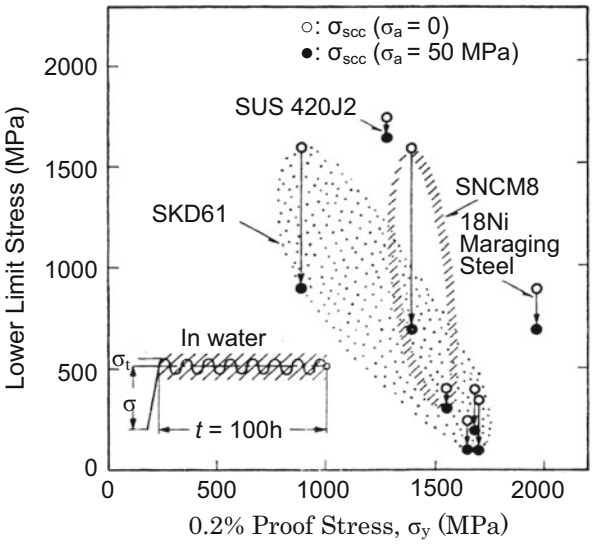

Fig. 6.26 Decrease in the lower limit stress by superposing cyclic variations of applied stress at sustained loading delayed fracture tests for various high strength steels (Kido et al. [58]. Reprinted with permission from The Iron & Steel Inst. Japan)

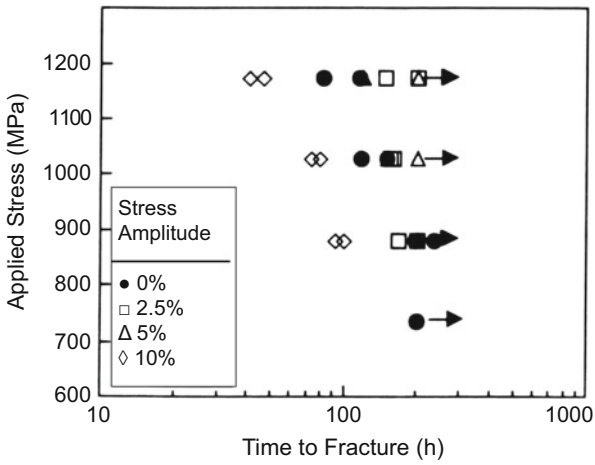

Fig. 6.27 Accelerated fracture by superposing cyclic stress variations at delayed fracture test of high strength steel. The maximum stress is constant (Izutsu et al. [59])

solution at 50 °C. Figure 6.27 [59] shows delayed fracture diagrams for various stress amplitudes. Promotion of fracture was evident at the stress amplitude of 10 % while the mean stress was lower than the constant stress level. A noteworthy finding was that hydrogen concentrations in tested specimens were uniquely determined by the immersion time in the solution irrespective of constant or cyclic stressing [59]. It implies that total hydrogen content is not the controlling factor for promoting fracture. The amount of lattice defects measured in terms of the amount of tracer-hydrogen introduced after the tests decreased when tested specimens were annealed at 200 °C. The decrease was larger for cyclic-stressed specimens than for sustained-loaded specimens. It indicates that cyclic stressing enhances creations of vacancies during the tests. Further studies on the effects of cyclic prestressing on tensile test and on interactions of fatigue and delayed fracture are presented in Sect. 7.3.2 concerning accumulation of damage.

(b) Environmental variations

Another factor to be examined for delayed fracture of structural components in service is variations of hydrogen fugacity associated with changes of weather. A laboratory method to examine effects of environmental variations on delayed fracture was to cyclically vary the hydrogen-charging current density [60]. Experiments were conducted for high strength martensitic steel of 1390 MPa in tensile strength in sustained-loading tests under concurrent hydrogen-charging. The specimens were round bars of 5 mm in diameter and hydrogen charging was conducted by a fairly mild cathodic electrolysis in a 3 % NaCl + 3 g/l NH_4SCN aqueous solution. The applied tensile stress was 70 % of the tensile strength, and the current density was cyclically varied from 0.1 to 100 cpm in a rectangular form keeping the maximum current density constant.

The time to fracture as a function of the frequency of cyclic currents is shown in Fig. 6.28 [60], where the maximum current density was 7.5 A/m^2 and the relative amplitude of the current variations was 10 %. Promoted failure by higher

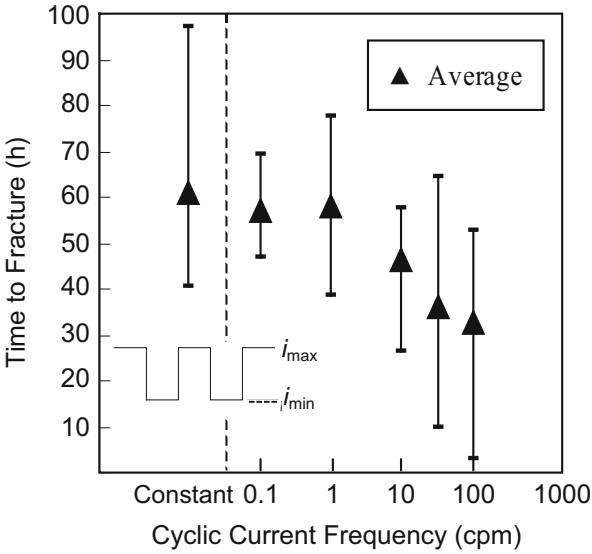

Fig. 6.28 Effects of cyclic variation of hydrogen-charging current density on the time to fracture at delayed fracture tests of high strength steel. The maximum current density is not varied (Nagumo et al. [60])

frequencies is evident. Hydrogen contents in unstressed specimens were uniquely determined by the total supplied electric charge irrespective of cyclic variations of the current density [60]. Subsequent analyses of trapped states of hydrogen by means of TDA revealed that TDA profiles changed with elapsed time of the test. The TDA profile showed a single broad peak centered at around 80 °C, but the higher temperature side of the peak showed a more pronounced increase with time. Similarly to the case of cyclic stress variation [59], alteration of TDA profiles with time appeared earlier for the cyclic current conditions than for the constant current test. The TDA results indicate the creation of trap sites of high binding energies. The low temperature thermal desorption spectroscopy (LTDS) shown in Figs. 3.9 and 3.10 ascribed the origin of such TDA profiles to vacancy clustering. The effects of environmental variations are consistently understood from the viewpoints of promoted vacancy clustering.

References

1. K. Takai, R. Watanuki, ISIJ Int. **43**, 520–526 (2003)
2. M. Hatano, M. Fujinami, K. Arai, H. Fujii, M. Nagumo, Acta Mater. **67**, 342–353 (2014)
3. I.M. Bernstein, in *Hydrogen Effects in Materials*, ed. by A.W. Thompson, N.R. Moody (TMS, Warrendale, 1996), pp. 3–11
4. T. Doshida, K. Takai, Acta Mater. **79**, 93–107 (2014)
5. K. Takai, H. Suzuki, M. Fujinami, *Reports on Construction of Fundamentals of Hydrogen Embrittlement* (Iron and Steel Inst., Japan, 2013), pp. 129–134
6. T. Nakamoto, T. Doshida, K. Takai, Y. Kubo, M. Fujinami, CAMP ISIJ **25**, 1210 (2012)
7. K. Takai, H. Shoda, H. Suzuki, M. Nagumo, Acta Mater. **56**, 5158–5167 (2008)

8. J.F. Knott, *Fundamentals of Fracture Mechanics* (Butterworth, London, 1973)
9. T.L. Anderson, *Fracture Mechanics*, 3rd edn. (Taylor & Francis, Boca Raton, 2005)
10. W.G. Clark Jr., J. Mater. Energy Syst **1**, 34–40 (1979)
11. R.A. Oriani, P.H. Josephic, Acta Metall. **22**, 1065–1074 (1974)
12. G.W. Simmons, P.S. Pao, R.P. Wei, Metall. Trans. A **9A**, 1147–1158 (1978)
13. W.W. Gerberich, Y.T. Chen, C. St John, Metall. Trans. A **6A**, 1485–1498 (1975)
14. J.F. Lessar, W.W. Gerberich, Metall. Trans. A **7A**, 953–960 (1976)
15. N.R. Moody, S.L. Robinson, W.M. Garrison, Res Mechanica **30**, 143–206 (1990)
16. Y. Takeda, C.J. McMahon Jr., Metall. Trans. A **12A**, 1255–1266 (1981)
17. J.A. Gordon, J.P. Hirth, A.M. Kumar, N.E. Moody Jr., Metall. Trans. A **23A**, 1013–1020 (1992)
18. S.V. Kamat, J.P. Hirth, Scr. Metal. Mater. **30**, 145–148 (1994)
19. Y. Fujii, A. Kikuchi, M. Nagumo, Metall. Mater. Trans. A **27A**, 469–471 (1996)
20. A. Needleman, W. Tvergaard, J. Mech. Phys. Solds **35**, 151–183 (1987)
21. Y. Shimomura, M. Nagumo, in *Environment-Induced Cracking of Materials: Chemistry, Mechanics and Mechanisms*, ed. by S.A. Shipilov, R.H. Jones, J.M. Olive, R.B. Rebak (Elsevier, Oxford, 2007), pp. 285–294
22. D.P. Williams, H.G. Nelson, Metall. Trans. **1**, 63–68 (1970)
23. R.P. Gangloff, R.P. Wei, Metall. Trans. A **8A**, 1043–1053 (1977)
24. H. Vehoff, W. Rothe, Acta Metall. **31**, 1781–1793 (1983)
25. H. Vehoff, H.-K. Llameth, Acta Metall. **33**, 955–962 (1985)
26. W.W. Gerberich, T. Livne, X.-F. Chen, M. Kaczorowski, Metall. Trans. A **19A**, 1319–1334 (1988)
27. M. Nagumo, H. Yoshida, Y. Shimomura, T. Kadokura, Mater. Trans. **42**, 132–137 (2001)
28. K.A. Nibur, B.P. Somerday, D.K. Balch, C. San Marchi, Acta Mater. **57**, 3795–3809 (2009)
29. M. Nagumo, T. Yagi, H. Saitoh, Acta Mater. **48**, 943–951 (2000)
30. R.W. Hertzberg, *Deformation and Fracture Mechanics of Engineering Materials*, 3rd edn. (Wiley, New York, 1989), Chapters 12, 13
31. W.W. Gerberich, in *Hydrogen Degradation of Ferrous Alloys*, ed. by R.A. Oriani, J.P. Hirth, M. Smialowski (Noyes Pub, Park Ridge, 1985), pp. 366–413
32. Y. Murakami, H. Matsunaga, Int. J. Fatigue **28**, 1509–1520 (2006)
33. M. Nagumo, H. Shimura, T. Chaya, H. Hayashi, I. Ochiai, Mater. Sci. Eng. **A348**, 192–200 (2003)
34. S. Suresh, G.F. Zamiski, R.O. Ritchie, Metall. Trans. A **12A**, 1435–1443 (1981)
35. S. Suresh, R.O. Ritchie, Scr. Metall. **17**, 575–580 (1983)
36. S.J. Hudak Jr., Trans. ASME J. Eng. Mater. Tech. **103**, 26–35 (1981)
37. M.H. Haddad, N.E. Dowling, T.H. Topper, K.N. Smith, Int. J. Fracture. **16**, 15–30 (1980)
38. S. Fukuyama, K. Yokogawa, M. Araki, J. Soc. Mater. Sci. Jpn. **34**, 709–714 (1985)
39. K.A. Esaklul, A.G. Wright, W.W. Gerberich, Scr. Metall. **17**, 1073–1078 (1983)
40. Y. Murakami, T. Kanezaki, Y. Mine, Metall. Mater. Trans. A **41A**, 2548–2562 (2010)
41. S. Ohmiya, H. Fujii, M. Nagumo, CAMP Iron Steel Inst. Jpn **25**, 1207 (2012)
42. J. Nakamura, M. Miyahara, T. Omura, H. Semba, M. Wakita, J. Soc. Mater. Sci. **60**, 1123–1129 (2011)
43. S. Stanzl, E. Tschegg, Acta Metall. **29**, 21–32 (1981)
44. Y. Murakami, H. Konishi, K. Takai, Y. Murakami, Tetsu-to-Hagané **86**, 777–783 (2000)
45. H.H. Johnson, J.G. Morlet, A.R. Troiano, Trans. Metall. Soc. AIME **212**, 528–536 (1958)
46. N. Suzuki, N. Ishii, T. Miyagawa, H. Harada, Tetsu-to-Hagané **79**, 227–232 (1993)
47. S. Yamazaki, T. Takahashi, Tetsu-to-Hagané **83**, 454–459 (1997)
48. Technical Report on Prestressing Steel 5: Fédération Int. Précontrainte (1980)
49. S. Yamamoto, T. Fujita, Kobe Steel Tech. Rep. **18**, 93–108 (1968)
50. W.W. Gerberich, Y.T. Chen, Metall. Trans. A **6A**, 271–278 (1975)
51. E.A. Steigerwald, F.W. Schaller, A.R. Troiano, Trans. Metall. Soc. AIME **215**, 1048–1052 (1959)

52. M. Nagumo, in *Fracture 1977, Proceedings of the 4th International Conference Fracture*, ed. by D.M.R. Taplin, vol. 3 (Univ. Waterloo Press, Waterloo, 1977), pp. 757–764
53. M. Nagumo, T. Tamaoki, T. Sugawara, in *Hydrogen Effects on Materials Behavior and Corrosion Deformation Interactions*, ed. by N.R. Moody, A.W. Thompson, R.E. Ricker, C.W. Was, K.H. Jones (TMS, Warrendale, 2003), pp. 999–1008
54. T. Kushida, ISIJ Int. **43**, 470–474 (2003)
55. M. Nagumo, M. Nakamura, K. Takai, Metall. Mater. Trans. A **32A**, 339–346 (2001)
56. T. Doshida, H. Suzuki, K. Takai, N. Oshima, T. Hirade, ISIJ Int. **52**, 198–207 (2012)
57. K. Nakasa, M. Kido, H. Takei, J. Jpn. Inst. Metals **40**, 744–751 (1976)
58. M. Kido, K. Nakasa, H. Takei, Tetsu-to-Hagané **65**, 535–541 (1979)
59. K. Izutsu, K. Takai, M. Nagumo, Tetsu-to-Hagané **83**, 371–376 (1997)
60. M. Nagumo, H. Uyama, M. Yoshizawa, Scr. Mater. **44**, 947–952 (2001)